# Appendix-B

# Severe Accident Analysis Report for MCCI

# TABLE OF CONTENTS

# LIST OF TABLES

## LIST OF FIGURES

## 1.0 INTRODUCTION

Molten corium-concrete interaction (MCCI) is a severe accident phenomenon occurring when corium is relocated from the vessel into the reactor cavity. The interaction involves melting and decomposition of concrete, chemical reactions between the concrete and corium materials, and heat transfer from the corium to its surroundings. It can potentially cause: a) a large amount of non-condensable and flammable gases being released from concrete decomposition; b) a large amount of heat due to the chemical reactions between the corium and the concrete; c) fission product release from the corium to the containment atmosphere; and d) significant amount of concrete erosion. Uranium dioxide, zirconium dioxide, zirconium and stainless steel comprise the core melt. The major constituents of concrete are $SiO_2$, CaO, $Al_2O_3$, MgO, $Fe_2O_3$, $K_2O$, $Na_2O$, free water, chemically bound water and $CO_2$. When the molten core material contacts the concrete and the temperature of the concrete reaches the ablation temperature the concrete begins to ablate and a layer of molten concrete or slag forms that separates the solid concrete below from the overlying core melt. The formation of the concrete melt may be accompanied by the appearance of a crust of core material that grows on the slag layer. Beneath the ablating surface of the concrete the solid concrete decomposes and releases water and $CO_2$ gas stored in the concrete. Thus gas bubbles evolve from the concrete ablation front and rise through the core melt pool. Portions of the concrete slag layer may be removed by the evolving gas bubbles and thereby enter and mix with the core melt. Since concrete is less dense than the overlying core melt material, buoyancy will also cause the concrete slag to rise and mix with the core melt. Thus the core melt pool is stirred by both gases and rising concrete slag. An intervening crust of frozen core material may temporarily impede or cut off the mixing of the concrete slag below the crust with the core melt pool above the crust.

As concrete slag continues to mix with the core melt pool additional complications arise. Core melt/concrete mixtures possess a wide temperature range between the liquidus and solidus temperatures where liquid and solid coexist. High viscosity conditions are likely to exist in the relatively cool boundary layers just above the concrete slag layer and beneath the surface of the pool. In these regions the core melt/concrete mixture temperature may be below the mixture liquidus temperature and at a point where the mixture carries a considerable quantity of precipitate solids. In fact, the whole MCCI pool may be at a temperature below the liquidus. Thus MCCI ablation heat transfer involves three phases: gas, liquid and solid. The viscosity of the mixture is known to increase sharply with increasing solids concentration (or, equivalently, decreasing temperature), making it difficult to assign an effective Newtonian viscosity to the mixture. The presence of a significant concentration of solids in core melt/concrete mixtures may cause foaming.

Most of the energy emitted by the pool's surface is transported to the containment walls or an overlying water pool via thermal radiation. However the surface temperature of the pool, which dictates the magnitude of the emitted radiation will be influenced by the presence of a crust cover, below-surface turbulent natural convection, and/or the passing of gas bubbles through the surface of the pool. Also, thermal radiation from the melt could be strongly attenuated by the particle cloud that obviously exists in the atmosphere above the pool. The MCCI process is sustained for a relatively long period of time by the radioactive decay of fission products and by a number of in-pool chemical reactions involving, say, the reduction of steam, $CO_2$ and $SiO_2$ by zirconium.

If there is any water in the reactor cavity, the underlying corium can be cooled by this water, and the released fission products can be scrubbed by the water pool. Therefore, MCCI in a flooded reactor cavity is generally less severe than MCCI in a dry cavity. However, heat transfer from corium to water can potentially generate a large amount of steam, in addition to the non-condensable gases generated during concrete decomposition, becoming another source of containment pressurization.

It is crucial to assess the consequences of MCCI and its threat to containment integrity to ensure that proper regulatory criteria are being satisfied. Specifically, for APR1400, there are two concerns with regard to MCCI: a) whether the containment pressure will exceed the containment failure pressure in the first 24 hours after core damage; and b) whether the concrete erosion will cause breach of the leak-tight boundary (liner) of the containment. The former means that the pressure in the containment does not exceed 123.7 psia (about 8.5 bar), as described in Section 2.1.2, Assumption 1. The latter means that the ablation in the containment floor concrete does not reach to the steel liner, which is located 3 feet (0.9 m) under the floor.

Clearly, the MCCI is a particularly difficult problem to deal with by mathematical modeling alone, and it was recognized early on that little progress would be made on this problem in the absence of experiments with prototypic reactor materials. Real material testing of the MCCI phenomenon began in 1975 and MCCI issue has continued unabated to this day. The early experiments as well as some recent ones involved metallic and oxidic melts poured onto concrete in the absence of an applied heat source. Later on emphasis was placed on the conduct of tests with sustained heating in the melt to simulate radioactive decay heating, but concrete ablation was limited to the downward direction only. Because sideward heat losses (ablation) from an MCCI pool is important in terms of the overall pool energy balance and because of the threat to containment structures in some plants, so called two-dimensional (2D) experiments were ultimately performed, which included both downward and sideward concrete ablation. Finally, the real material MCCI test included flooding the interacting materials from above with water to see if the MCCI could be terminated by quenching.

## 2.0 ANALYSIS METHODOLOGY

Integral severe accident analysis code MAAP 4.0.8 was used to calculate the containment pressure and concrete floor and side ablation depths through MCCI phenomena for APR1400 plant under severe accident scenarios. This section discusses the assumptions and main features of the MAAP 4.0.8 model, followed by quantifications of key modeling parameters FCHF and ENT0C.

### 2.1 Major Assumptions

#### 2.1.1 MAAP 4.0.8 MCCI Model

The following assumptions were used in the MCCI model in MAAP 4.0.8 (Reference 1) to simplify the complexity of the physical and chemical processes:

1) The corium is homogeneously mixed due to the agitation by the off-gases from concrete ablation, i.e., no stratification is considered in the corium.

2) The corium pool is represented by a single average internal energy.

3) The oxide corium is treated as a pseudo-binary system of core oxides ($UO_2$, $ZrO_2$) and concrete oxides ($SiO_2$, CaO, MgO, $Al_2O_3$, etc.).

4) Chemical reactions can be treated by an equilibrium model.

5) Corium crust has the same composition as molten debris.

6) Temperature distribution in the crust is close to steady-state profile.

7) All energy involved in the concrete phase change and endothermic chemical reactions can be lumped together as a single effective latent heat.

8) The temperature profile in the concrete slab is essentially one-dimensional in the direction of erosion. Fine nodes are used near the erosion interface to track the melting front.

9) Gases released from the concrete floor ablation will enter the corium mixture at 100%. Gases released from the (vertical) concrete sidewall ablation will also enter the corium mixture at a user specified fraction.

10) The heat transfer rate from the corium to water above it is given by a formulation for CHF rate, which can be adjusted by a user specified parameter FCHF.

11) The reactor cavity floor is a flat one-piece concrete slab, i.e., it has no deep concaving part such as sump.

### 2.1.2 Other

1) The containment pressure failure criterion for the period 24 hours after core damage is assumed to be 123.7 psia based on containment performance analysis. SECY-93-087 (Reference 12) requires that the Factored Load Category (FLC) requirements of the ASME Boiler and Pressure Vessel Code, Section III, Division 2 need to be satisfied. Based on subarticle CC-3720, this means that the liner strain must remain below 0.003. The assumed pressure failure criterion (123.7 psia) results in liner strain below 0.003 and thus is conservative compared to the requirements of SECY-93-087. The assumed pressure limit will be referred to as the "FLC" throughout this report.

## 2.2 Main Features of MCCI Model

Figure 2-1 illustrates how MAAP 4.0.8 models the interaction between corium and its surrounding in the reactor cavity. Specifically, it models corium contacting a concrete floor and sidewall, while losing heat by boiling heat transfer to water if the cavity is flooded or by thermal radiation to upper walls and by convection to the atmosphere if the cavity is dry. The floor and sidewall are modeled as one horizontal and one vertical heat sink that can be ablated by, and react with the corium pool. As the concrete heat sink ablates, it releases decomposed non-gaseous constituents, namely "slag", and gaseous constituents, namely "off-gases", which enter the corium pool and react with corium materials to generate heat and gases such as CO and $H_2$.

### 2.2.1 Corium Thermal Property Evaluation

One of the evaluations in MCCI model is to determine thermal properties in the corium mixture based on bulk constituents and total internal energy, including temperature, solid fraction, viscosity, and other properties. MAAP 4.0.8 follows a simplified approach, including partitioning the elements into oxidic and metallic phases, constructing pseudo-binary phase diagram, and finding the temperature and other properties.

#### 2.2.1.1 Element Partition

Corium in the reactor cavity typically consists of $UO_2$, Zr, $ZrO_2$, Fe, Cr, Ni, either $B_4C$ or Ag-In-Cd plus fission product compounds (such as SrO, BaO, $La_2O_3$, etc.) and trace materials contained in alloys (such as Sn, Mn, etc.). It also includes the compounds from concrete slag (such as $SiO_2$, CaO, MgO, etc.) as the molten core-concrete interaction progresses. The compounds in the corium can form solutions in which the oxygen initially associated with oxides is partly dissolved in a metallic phase and partly remains in an oxidic phase. Other elements, such as U would be preferentially present in the oxide phase, while Fe, Cr and Ni, would be preferentially present in the metallic phase. In general, every element will partition in some proportion between these two phases.

If material data was available for an applicable range, an equilibrium calculation could be used to evaluate the composition of the metal and oxide phases by minimizing the Gibbs free energy of both phases at constant temperature. Unfortunately, functional forms for chemical potentials (Gibbs free energies) have only been created for a small subset of the compounds of interest, namely $UO_2$,

$ZrO_2$, $SiO_2$, CaO, and MgO. Thus, a rigorous model cannot be applied to the entire corium system. However, it can be applied to some subsystems to yield pseudo-binary data.

A simplification was made to replace the free energy minimization calculations with two types of data: equilibrium compositions within each phase as a function of temperature and bulk composition (a phase diagram for each phase), and internal energy functions for each compound in each phase (enthalpies of mixing). The means of combining these data constitute the solution technique for temperature, either for each phase separately or for both phases isothermally. Figure 2-2 illustrates how various elements are expected to be partitioned between metal and oxide phases of core debris. MAAP 4.0.8 assumes that U and Zr will essentially oxidize to completion before $B_4C$, Fe, Cr, and Ni begin to oxidize. It also assumes that reduction of slag oxides such as $SiO_2$ and CaO may be neglected for the temperature calculation. PWR control rod material constituents Ag-In-Cd (minor metals) are excluded from the metal phase diagram because they are assumed to have a negligible influence compared to other materials; however, their internal energy is considered. Trace materials such as Sn and Mn are assumed to have both negligible energy and influence on the phase equilibriums, and are excluded from the phase diagrams and the temperature calculation.

Materials defined for the energy calculation are therefore:

1) U-Zr-O + (SO + CN): Oxides, a combination of U-Zr-O, steel oxides and concrete slag oxides;

2) BCS: Major metals, a combination of B-C-Fe-Cr-Ni-Zr;

3) Ag-In-Cd: Minor metals for PWR control materials.

#### 2.2.1.2 Phase Diagrams

For oxidic phase, core-concrete oxides are characterized by a large difference in the melting range between core debris (typically between 2900 K to 3100 K) and concrete slag (typically 1300 K to 1700 K). The pseudo-binary phase diagram approach has therefore been applied to this system using core oxide and concrete slag as two pseudo-compounds.

Based on the best-estimate calculations for a core-oxide – concrete-oxide pseudo-binary system (Reference 3) a generic core-concrete pseudo-binary phase diagram, as shown in Figure 2-3 is developed. The solidus and liquidus of each pseudo-compound and the solidus, liquidus, and liquid fraction for the mixture of the two pseudo-compounds are shown as a function of composition and temperature. Key parameters of the phase diagram of core-oxide – concrete are user inputs in the concrete property section of MAAP 4.0.8 parameter file.

The energy-temperature constitutive relationship for a pseudo-binary oxide mixture is plotted in Figure 2-4. Given the composition and selecting a temperature, one can obtain the liquid fraction, and solidus and liquidus temperature by interpolation. The oxide mixture energy is then given by:

$$U = (1 - f_L)\sum_i X_{iS} U_{iS} + f_L \sum_i X_{iL} U_{iL} \quad (2\text{-}1)$$

where U is the energy, $X_{iS}$ and $X_{iL}$ are the solid and liquid composition of component i respectively, and $f_L$ is the liquid mass fraction.

For metallic phase, it is assumed that the metal phase can be represented as a pseudo-binary mixture of Fe plus other metals, for three reasons. First, unless large quantities of un-oxidized Zr are present, Fe will be by far the most abundant metal. Second, even when there is more Zr than Fe, the amount of other metals (except U) relative to Fe would be small and hence a binary Fe-Zr (or pseudo-binary Fe-(U,Zr)) diagram may be a good first approximation to the real system. Last, binary Fe - other metal phase diagrams are commonly available.

The pseudo-binary phase diagram can be generated from binary metal phase diagram data. It is assumed that dissolved oxygen has a negligible impact on the metal phase diagram. This is a good approximation when Fe dominates the metals, though it is not as clearly valid for Zr. Therefore, dissolved oxygen will only be considered to influence the melting point of otherwise pure Zr. The calculated phase diagram for the metal phase is shown in Figure 2-5.

The temperature-energy relationship for the metallic phase is assumed to be the same as for the oxides, except that there is no congruent melting at the liquidus, or the solidus.

#### 2.2.1.3 Temperature Calculating Procedure

Given the energy and composition of the corium mixture, MAAP 4.0.8 determines its temperature with the phase diagram. The first step is to find the phase change temperatures, i.e., the solidus and the liquidus, for each of the three pseudo-compounds: the oxide, the major metal, and the minor metal. The energy of each material at phase change is obtained from the “pure” substance material properties. Total energy of the mixture at each phase change temperature is then calculated as the sum of energies of all materials.
To find the upper and lower bounds of temperature for the iteration, input energy is compared with the mixture total energy at every phase change temperature. When input energy is between the upper and lower bounds of a phase change, the temperature is known and the solid fraction can be directly solved. When the mixture input energy is between the phase change energies at two temperatures, Newton's method is applied to find the temperature iteratively. A linear programming method is used to find the temperature if Newton's method does not converge within the expected number of iterations.

Once the temperature is determined, properties of the corium such as density, volume, and viscosity are determined from averaging those of individual constituents.

### 2.2.2 Corium - Concrete Chemical Reactions

Chemical reactions between the concrete and corium materials are the major cause generating large amount of heat and non-condensable gases, including the combustible gases of $H_2$ and CO. The chemical reactions are calculated by a module in the MAAP 4.0.8 model that assumes chemical equilibrium reached at each time step.

Table 2-1 lists the reactions and the basic chemical species considered in the model. In addition to the basic species listed in Table 2-1, a number of intermediate (auxiliary) species shown in Table

2-2 are also considered. At the equilibrium, the partial pressures of the reactants and products follow a temperature dependent ratio. An example is given here for the reaction of $H_2$ plus $CO_2$ to generate $H_2O$ and CO (equation 1 in Table 2-1):

$$k_1 = \frac{p(H_2)\, p(CO_2)}{p(H_2O)\, p(CO)} \tag{2-2}$$

where $k_1$ is a temperature-dependent chemical reaction ratio evaluated at each time step, and p( ) designates the partial pressure of a particular species in the mixture. Taking the natural logarithm of each side and noticing that the total pressure and total number of gas moles cancels out, p can be replaced by n, or the number of moles, yielding:

$$r_1 = 0 = -\ln(k_1) + \ln[n(H_2)] + \ln[n(CO_2)] - \ln[n(H_2O)] - \ln[n(CO)] \tag{2-3}$$

where $r_1$ is the residual function for the first basic species. Similar equations can be written for all the basic species and auxiliary species. Ultimately, Newton-Raphson technique can be used to find the number of mole for each species that reduces the residual function r to zero.

Through this technique, the compositions at the equilibrium are solved at each time step based on the instantaneous temperature, and the heat and gases generations are determined by comparing the current time step equilibrium compositions and the previous time step compositions. The non-condensable gases released from the chemical reactions are added to containment gas space to assess pressurization rate in the containment.

### 2.2.3 Concrete Ablation

Ultimately, the objective of MCCI studies is to evaluate the potential failing the containment integrity, either through too much concrete ablation, or too much pressurization. The evaluation must be performed by calculating the heat transfer from the corium into the concrete and concrete ablation rate.

If the corium-concrete mixture pool is substantially deep to prevent removal of the heat generated by fission product through conduction, the central region of the pool remains molten. Three pieces of solid crusts are tracked, including: the lower crust interacting with the concrete floor, the side crust interacting with the concrete sidewall, and the upper crust at the top transferring heat to water, gas or reactor cavity upper wall heat sink. Each crust may have different thickness depending on the convective heat transfer from the molten pool to the crust, and from the crust to its interfaced heat sink. The heat flux from the molten pool to the crust can be represented by the convective term given in the following equation

$$q'' = \begin{cases} h_d\left(T_F - T_{F,m}\right) & \text{, for bottom crust} \\ h_s\left(T_F - T_{F,m}\right) & \text{, for side crust} \\ h_u\left(T_F - T_{F,m}\right) & \text{, for upper crust} \end{cases} \tag{2-4}$$

where q" is the heat flux from the molten pool to the crust, $h_d$, $h_s$ and $h_u$ are the downward, sideward and upward heat transfer coefficients, $T_F$ is the bulk temperature of the molten debris, and $T_{F,m}$ is the melting temperature of the debris. The convective heat transfer coefficient is affected by

viscosity, and the viscosity increases rapidly with increasing debris solid fraction. The solid fraction of the oxide debris can be treated as a pseudo-binary system of core oxide ($UO_2$, $ZrO_2$) and concrete oxide ($SiO_2$, CaO, MgO, $Al_2O_3$, etc.). As discussed in the previous section, the solid fraction is governed by the system temperature, which, in turn, is controlled by the heat transfer from the pool. When the pool is 100% liquid, the maximum convective heat transfer is achieved, and when the debris is completely solidified, the convective term disappears. Downward, sideward, and upward heat transfer coefficients are modeled as functions of the corium solid fraction, expressed by the following mathematical formulation:

$$h_i = h_{i,0}\left(1 - f_s\right)^n \tag{2-5}$$

where subscript i represents downward (i=d), sideward (i=s) or upward (i=u) heat transfer coefficient, $h_{x,0}$ is the nominal maximum value of the coefficient, $f_s$ is the solid fraction in the molten pool, and n is an exponent. Experimental data were used to determine the nominal heat transfer coefficient and the exponent.

Heat transfer from the crust to its interfaced heat sink is calculated with the assumption that the temperature distribution in the crust is close to the steady-state profile. Due to internal heat generation, the steady-state profile in the crust is a parabolic function. The exact temperature distribution is determined with the boundary conditions at the interfaces between the molten pool and the crust, and between the crust and heat sink. In most cases, the temperature between the interface of the molten pool and the crust stays at the corium melting (solidus) temperature; the temperature between the interface of the crust and concrete is at the concrete melting temperature. Once the temperature profiles are evaluated with the given boundary conditions of the temperatures at the interfaces, the crust growing or shrinking rate is evaluated through energy balance, given as

$$\frac{dX_{cr,i}}{dt} = \frac{q_i'' + q_v''' X_{cr,i} - k_{cr}\left.\frac{dT_{cr,i}}{dx}\right|_{x=X_{cr,i}}}{\rho_{cr} LH_{cr}} \tag{2-6}$$

where $X_{cr,i}$ is the thickness of crust, $q_i''$ is the convective heat transfer rate from the molten corium pool to the crust, $q_v'''$ is the volumetric decay power generation rate in the crust, $k_{cr}\left.\frac{dT_{cr}}{dx}\right|_{x=X_i}$ term represents the heat conduction rate from the crust to the concrete, $\rho_{cr}$ is the density of the crust, $LH_{cr}$ is the latent heat from the crust to form or melt. Based on the temperature profile, the heat flux from the crusts to the heat sinks $q_{cn}''$ is easily evaluated through conduction heat transfer equations.

Once the energy loss to the concrete $q_{cn}''$ is determined, response of the concrete material to the imposed heat flux is solved by considering energy balance at the ablation front. The concrete heat sink is modeled as one-dimensional slab, and the temperature distribution in the slab is simulated with a fully implicit solution of the one-dimensional heat conduction equation. For a given the heat flux from the core debris into the concrete, its ablation rate is calculated through the energy balance as:

$$\frac{dX_{cn,i}}{dt} = \frac{q_{cn,i}'' - k_{cn}\left.\frac{dT_{cn,i}}{dx}\right|_{x=0}}{\rho_{cn} LH_{cn}} \quad (2\text{-}7)$$

where $\frac{dX_{cn,i}}{dt}$ is the ablation rate $T_{cn,i}$ is the temperature in the concrete slab, $k_{cn}\left.\frac{dT_{cn,i}}{dx}\right|_{x=0}$ is the heat flux conducted away from the interface, $\rho_{cn}$ is the concrete density. The latent heat term $LH_{cn}$ is a bulk latent heat of concrete including the latent heat for both melting and decomposition processes.

### 2.2.4 Effects of Water

Corium-water interaction is a model separate from MCCI in MAAP 4.0.8. However, MCCI severity can be substantially reduced by a large amount of water in the cavity, and the heat transfer rate evaluation between corium and water has a significant impact on MCCI progression.
Two phenomena can be identified for corium-water interaction from an MCCI perspective: initial jet breakup, and water ingression. First, initial jet breakup is the phenomenon occurring when a corium jet forms between the vessel and the bottom of a deep water pool. Corium particles can be stripped off from the corium jet due to intensity of the corium-water interaction. These particles can eventually settle on top of the upper crust of corium pool, forming a layer known as the particle bed. As a result of this process, the mass of the molten corium pool can be significantly reduced, making the MCCI less severe. Second, water ingression is the phenomenon occurring once corium is fully settled on top of the cavity floor. As the corium is covered by water, the large heat removal from the top surface can produce a thick upper crust. According to experimental data, heat removal rate by water in this configuration would by far exceed the maximum heat transfer rate through the upper crust layer, if the layer were continuous and impermeable. The upper crust is not a continuous, impermeable layer; instead, numerous deep cracks can develop, as the solidified corium in the upper crust is subjected to a large temperature gradient. Water and steam can ingress (infiltrate) into the corium through these cracks, contacting the hotter region of the corium. As the solidification progresses, both the temperature gradient and the cracks extend deeper into the corium pool.

The model in MAAP 4.0.8 evaluates the heat transfer and oxidation of metal during the process of the initial jet breakup. However, it does not simulate the formation of the particle bed on top of the upper crust. MAAP 4.0.8 assumes that the particles formed during the initial jet breakup are promptly merged into the corium pool. The mass stripping rate off of a jet is calculated using a formulation similar to the Ricou-Spalding model (Reference 4):

$$\frac{dr_{dj}}{dt} = ENT0C \cdot \left(\frac{\rho_w}{\rho_{dj}}\right)^{1/2} u_{dj} \quad (2\text{-}8)$$

where $r_{dj}$ is the radius of the corium jet, $\rho_w$ is the density of water, $\rho_{dj}$ is the density of corium jet, and $u_{dj}$ is the velocity of the corium jet. Model parameter ENT0C is a coefficient multiplier to the total

mass of stripped particles (the higher the coefficient, the larger the fraction is). The recommended range for the parameter ENT0C in the MAAP 4.0.8 code is from 0.025 to 0.06 (Reference 1).

MAAP 4.0.8 models water ingression by assuming the heat flux from a corium pool to its overlying water is prescribed by CHF heat flux, or higher, because water always ingresses into the hot region in the corium. The heat flux formulation is given by:

$$q''_{cr-wt} = FCHF \cdot \left[ \frac{g\sigma(\rho_l - \rho_g)}{\rho_g^{\,2}} \right]^{1/4} \rho_g (h_g - h_l) \qquad (2\text{-}9)$$

where g is the gravity constant, $\rho_l$ and $\rho_g$ are densities of saturated water and steam, and $h_l$ and $h_g$ are enthalpies of saturated water and steam. Modeling parameter FCHF is the Kutateladze number (Reference 5) for corium to water heat transfer, which controls the magnitude of the heat flux. The recommended of values for FCHF is from 0.0036 to 0.3.

### 2.3 MAAP 4.0.8 Model Limitations

The MCCI model in MAAP 4.0.8 was created and benchmarked against experiments designed for a dry cavity case (Reference 1), where the corium is mostly homogeneous in terms of temperature, geometry, and composition. For this case, assumptions and methodology of the MCCI model in MAAP 4.0.8 work reasonably well compared with the experiments. However, for a wet cavity case, the model has several limitations: one is that the MAAP 4.0.8 model does not consider the effects of melt eruption, which occurs when corium is ablating a type of concrete with rich gaseous constituents, such as Limestone or Limestone Common-Sand concrete. In this case, the released off-gases from concrete can entrain the molten corium into particles, and carry those particles through many ventilation channels (eruption sites) to the top of the upper crust. A number of experiments have confirmed the phenomenon of melt eruption (Reference 6, Reference 7, and Reference 8). The significance of this phenomenon is that it transforms portions of the continuous corium pool into a particle bed, which is much more easily cooled by the overlying water. The second limitation is that the MAAP 4.0.8 model does not address the particle bed formed by melt eruption and/or initial jet breakup. As discussed in the section 2.2.4, MAAP 4.0.8 considers heat transfer and metal oxidation during the jet breakup, but it does not consider the particle bed formed by the particles stripped off from the corium jet or entrained by off-gases during melt eruption. The heat transfer from the particle bed to water is thus not a part of the corium and water interaction model. The third limitation of MAAP 4.0.8 is that it assumes a homogeneous corium pool (assumption 1 and 2 in the section 2.1). The homogeneous assumption in the MAAP 4.0.8 code causes all the layers (molten pool and crusts at the top, bottom, and sides) to be lumped into one pool, having a single average temperature, which may lead to an optimistic prediction of the time to completely quench (solidify) the corium. However, a corium pool can develop a thick, quenched upper crust, with a much lower temperature than the molten pool, when a large amount of water is in the cavity. On top of this crust, a particle bed can form. Essentially, experimental data (Reference 9) support a stratified geometry of the corium, with a particle bed at the top, a thick upper crust in the middle, and a molten pool at the bottom.

In addition to the limitations in wet cavity scenarios, the MAAP 4.0.8 model has limited capabilities of modeling a reactor cavity with a sump in its floor. In this case, the corium pool in the sump has a

different cross-section area from the pool in the remaining cavity, and the walls and the floor in the sump may be subject to deeper ablation than the remaining cavity walls and floor. The way for MAAP 4.0.8 to handle such geometry is to split the corium pool in the cavity into two: one in the sump, and the other in the remaining part of the cavity.

For calculations presented herein, the MAAP 4.0.8 model limitations for the wet cavity scenario are accommodated by calibrating the two model parameters FCHF and ENT0C discussed in section 2.2.4. The objective is to have MAAP4.0.8 generating conservative results in terms of key variables. Model parameter FCHF is adjusted based on the results calculated by more sophisticated MCCI codes. This will allow for conservative predictions of ablation depth and long term containment pressurization. However, time required to completely quench the corium pool may not be correctly predicted, and it must be obtained through experiments or other more sophisticated codes. Details of calibrating FCHF and ENT0C are given in the next section.

The model limitation of the cavity floor geometry with a sump is not handled in this analysis report. Detailed CORQUENCH calculations show that the corium in the sump is quenched before the ablation depth reaches the liner plate. (Reference 10)

### 2.4 Quantifications of Key Inputs

For the MCCI cases considered in this analysis report, default and case specific inputs for running the MAAP 4.0.8 code have been documented in the parameter file and input decks for APR1400. Besides these default inputs, two key modeling parameters, FCHF and ENT0C, must to be calibrated to accommodate the modeling deficiency discussed in the previous section. The objective in selecting the parameter values is to conservatively predict the key variables important to containment performance of APR1400. These include the ablation depth in the cavity floor and the containment pressure 24 hours after core damage. The code chosen as the basis for calibration of MAAP 4.0.8 model parameters is CORQUENCH 3.03 (Reference 10), which is a MCCI code developed by Argonne National Laboratory. This code models a stratified corium pool structure consisting of an upper crust, a bottom crust, and a molten pool; it also models the effects of melt eruption.

#### 2.4.1 CORQUENCH 3.03 Results

CORQUENCH 3.03 analysis was performed by Argonne National Laboratory, for Siliceous, and LCS (Limestone and common sand) concrete types. The initial conditions used in these calculations are summarized as the following:

1) Sequence initiator is a Large LOCA. To add more conservatism, core support plate is assumed to fail at about 6000 seconds, dumping the entire core into the RPV lower plenum. Reactor vessel fails at about 7100 seconds.

2) About 118 tons of $UO_2$ and 29.6 tons of Zr are relocated from the vessel into the cavity, which correspond to 100% of inventory in the core.

3) Oxidation fraction of Zr is about 52%

4) Initial temperature of the melt is about 2500 K

The CORQUENCH 3.03 calculation is based on a very conservative assumption, which ignores the particle bed created during the initial jet breakup phase. This means that the particle bed can only be created through melt eruption when MCCI occurs. CORQUENCH 3.03 calculation also assumes that the containment pressure stays at a constant pressure of 1 bar during the entire MCCI process due to activation of containment sprays. The results indicate that the corium is quenched in about 8 hours and the ablation depth of the concrete floor is about 27 cm. The average heat flux from the corium pool to water is about 415 $kW/m^2$ during MCCI.

### 2.4.2 Selection of the FCHF Value

Several MAAP 4.0.8 cases were run with different values of FCHF to compare with the results of CORQUENCH 3.03. The whole core is modeled to relocate into the cavity at the time of vessel failure for MAAP 4.0.8, the same as for the other two codes. Parameter ENT0C is set to $1\times10^{-5}$ to disable the effect of jet breakup. Containment sprays are assumed unavailable to allow the containment pressure to increase. Figure 2-6 to Figure 2-9 shows ablation depths, total heat transferred from corium to water, and containment pressures for different FCHF values.

For LCS concrete, Figure 2-6 indicates that FCHF=0.0235 causes an ablation depth of 36 cm. Compared to the CORQUENCH results, MAAP4.0.8 result adds more conservatism to the ablation depth.

Figure 2-7 indicates that after vessel failure, FCHF=0.0365 causes a heat flux from corium to water of about 415 $kW/m^2$, which is close to the heat flux calculated by CORQUENCH.

In terms of containment pressure, Figure 2-9 indicates that for FCHF greater than 0.02, containment pressures do not differ significantly at the end of simulations, or 100,000 seconds (about 28 hours). This is because MAAP 4.0.8 models the same total heat transfer from corium to water both before, and after the corium average temperature drops below the water saturation temperature. As the corium is just relocated from the core, its temperature is significantly higher than the water saturation temperature. In this case, the heat transfer rate from corium to water is controlled by the value of FCHF, and a higher FCHF leads to a higher heat transfer rate, as shown in the Figure 2-8. However, the corium average temperature will eventually drop close to water saturation temperature. In this case, the MAAP 4.0.8 model considers that all sensible heat within the corium is gone, and the heat transfer from corium to water is controlled by decay power, not by FCHF. This transition is represented in Figure 2-8 by a drop in the power transfer from corium to water. Therefore, higher FCHF values simply cause the corium temperature to reach water saturation temperature faster, followed by a drop of the heat transfer rate. However, the total energy transferred into the water does not change much for different values of FCHF. This indicates that containment pressurization is only a weak function of FCHF in the long term.

### 2.4.3 Selection of the ENT0C Value

Another key input parameter that needs to be determined is the jet breakup coefficient ENT0C. It has been set to a small number ($1\times10^{-5}$) in MAAP runs being compared with CORQUENCH 3.03 results (see section 2.4.2). The concern with setting this parameter to a small number instead of its default value of 0.045 is that, ignoring the effects of the initial jet breakup also fails to capture the steam and hydrogen generations caused by quenching the stripped off corium particles at the time of reactor vessel failure. To quantify the magnitude of the pressure rise caused by the jet breakup,

two more MAAP 4.0.8 runs were executed with FCHF=0.0235: one with ENT0C=$10^{-5}$, and the other with a default value of ENT0C=0.045. Figure 2-10 shows the containment pressure comparison for these two runs, which indicates that the pressure rises only about 0.17 bar for the sequence with ENT0C=0.045. Considering that the MAAP runs described in this section conservatively assume that the entire core is dumped into the cavity at the time of vessel failure, the pressure difference between the sequences with a large and a small value of ENT0C is insignificant. When changing ENT0C, major differences are not likely to occur in pressure change, but in ablation depth.

### 2.4.4 Summary of MCCI Parameters Used in MAAP 4.0.8 Analyses for APR1400

Table 2-3 and Table 2-4 show two sets of values for MCCI parameters, FCHF and ENT0C. The set of parameters in Table 2-3 leads to conservative results for ablation depth and containment pressure within 24 hours of core damage, as discussed in the previous two sections. Therefore, for all the APR1400 MAAP4.0.8 analyses, both in this and other analysis, this set of MCCI parameters is used.

The second set of MCCI parameters (listed in Table 2-4) has the merit to capture the rapid steam and hydrogen generation occurring right after vessel failure. This set of parameters impacts the potential of local high hydrogen concentration and DDT. Therefore, all the severe accident sequences are additionally analyzed with this set of parameters, for the hydrogen analysis.

**Table 2-1: Basis Equations and Species**

| | | |
|---|---|---|
| 1. | $H_2$ | $H_2 + CO_2 \leftrightarrows H_2O + CO$ |
| 2. | C | $C + H_2O \leftrightarrows CO + H_2$ |
| 3. | Zr | $Zr(1) + 2H_2O \leftrightarrows ZrO_2(1) + 2H_2$ |
| 4. | Cr | $2Cr(1) + 3H_2O \leftrightarrows Cr_2O_3(1) + 3H_2$ |
| 5. | Fe | $Fe(1) + H_2O \leftrightarrows FeO(1) + H_2$ |
| 6. | $SIO_2$ | $SiO_2(1) + H_2 \leftrightarrows SiO + H_2O$ |
| 7. | CaO | $CaO(1) + H_2 \leftrightarrows Ca + H_2O$ |
| 8. | $Al_2O_3$ | $Al_2O_3(1) + 3H_2 \leftrightarrows 2Al + 3H_2O$ |
| 9. | $K_2O$ | $K_2O(1) + H_2 \leftrightarrows 2K + H_2O$ |
| 10. | $H_2O$ | Hydrogen element balance |
| 11. | CO | Oxygen element balance |
| 12. | $CO_2$ | Carbon element balance |
| 13. | $Cr_2O_3$ | Chromium element balance |
| 14. | FeO | Iron element balance |
| 15. | $B_4C$ | $B_4C(1) + 7H_2O \leftrightarrows 2B_2O_3(1) + CO + 7H_2$ |
| 16. | $UO_2$ | $UO_2(1) + 2H_2 \leftrightarrows U(1) + 2H_2O$ |
| 17. | $O_2$ | $H_2O \leftrightarrows H_2 + 1/2\ O_2$ |
| 18. | KOH | Potassium element balance |
| 19. | $B_2O_3$ | Boron element balance |
| 20. | Ni | $Ni(1) + H_2O \leftrightarrows NiO(1) + H_2$ |
| 21. | NiO | Nickel element balance |
| 22. | H | $H_2 \leftrightarrows 2H$ |
| 23. | Silicon element balance | |

**Table 2-2: METOXA Compound List**

| | Liquid Metals | Liquid Oxides | Gases | | | |
|---|---|---|---|---|---|---|
| 1. | $H_2$ | $H_2O$ | O2 | OH | H | O |
| 2. | C | | CO | $CO_2$ | | |
| 3. | Zr | $ZrO_2$ | ZrO | $ZrO_2$ | | |
| 4. | Cr | $Cr_2O_3$ | Cr | CrO | $CrO_2$ | $CrO_3$ |
| 5. | Fe | FeO | Fe | $Fe(OH)_2$ | | |
| 6. | | $SiO_2$ | SeO | $Si_3$ | | |
| 7. | | CaO | Ca | CaOH | $Ca(OH)_2$ | |
| 8. | | $Al_2O_3$ | Al | $Al_2O$ | AlOH | $Al(OH)_2$ |
| 9. | | $K_2O$ | K | KOH | | |
| 10. | | $Na_2O$ | Na | NaOH | | |
| 11. | Ni | NiO | Ni | NiH | $Ni(OH)_2$ | |
| 12. | $B_4C$ | $B_2O_3$ | BO | $B_2O_3$ | $BO_2$ | |
| 13. | Ag | | Ag | AgH | | |
| 14. | In | | In | | | |
| 15. | Cd | | Cd | | | |
| 16. | Sr | SrO | Sr | SrOH | $Sr(OH)_2$ | |
| 17. | Ba | BaO | Ba | BaO | BaOH | $Ba(OH)_2$ |
| 18. | La | $La_2O_3$ | LaO | $La(OH)_2$ | | |
| 19. | Ce | $CeO_2$ | CeO | $CeO_2$ | | |
| 20. | U | $UO_2$ | UO | $UO_2$ | $UO_3$ | $UO_2(OH)_2$ |
| 21. | | MgO | Mg | MgOH | $Mg(OH)_2$ | |
| 22. | Sn | $SnO_2$ | Sn | SnH | SnO | |
| 23. | Mn | MnO | Mn | MnH | $Mn(OH)_2$ | $H_2MoO_4$* |
| 24. | Mo | $MoO_2$, $MoO_3$ | | Mo | $MoO_2$ | $MoO_3$ |
| 25. | Ru | | Ru | RuO | $RuO_3$ | |
| 26. | Te | | Te | SnTe | AgTe | SbTe |
| 27. | Nb | NbO, $NbO_2$ | | NbO | $NbO_2$ | |
| 28. | Sb | | Sb | SbO | | |

* There are 7 total Mo compounds.

**Table 2-3: MCCI Parameters Used in MAAP4.0.8 Analyses for APR1400**

TS

**Table 2-4: Additional Set of MCCI Parameters Used in Hydrogen Distribution and DDT Analyses for APR1400**

TS

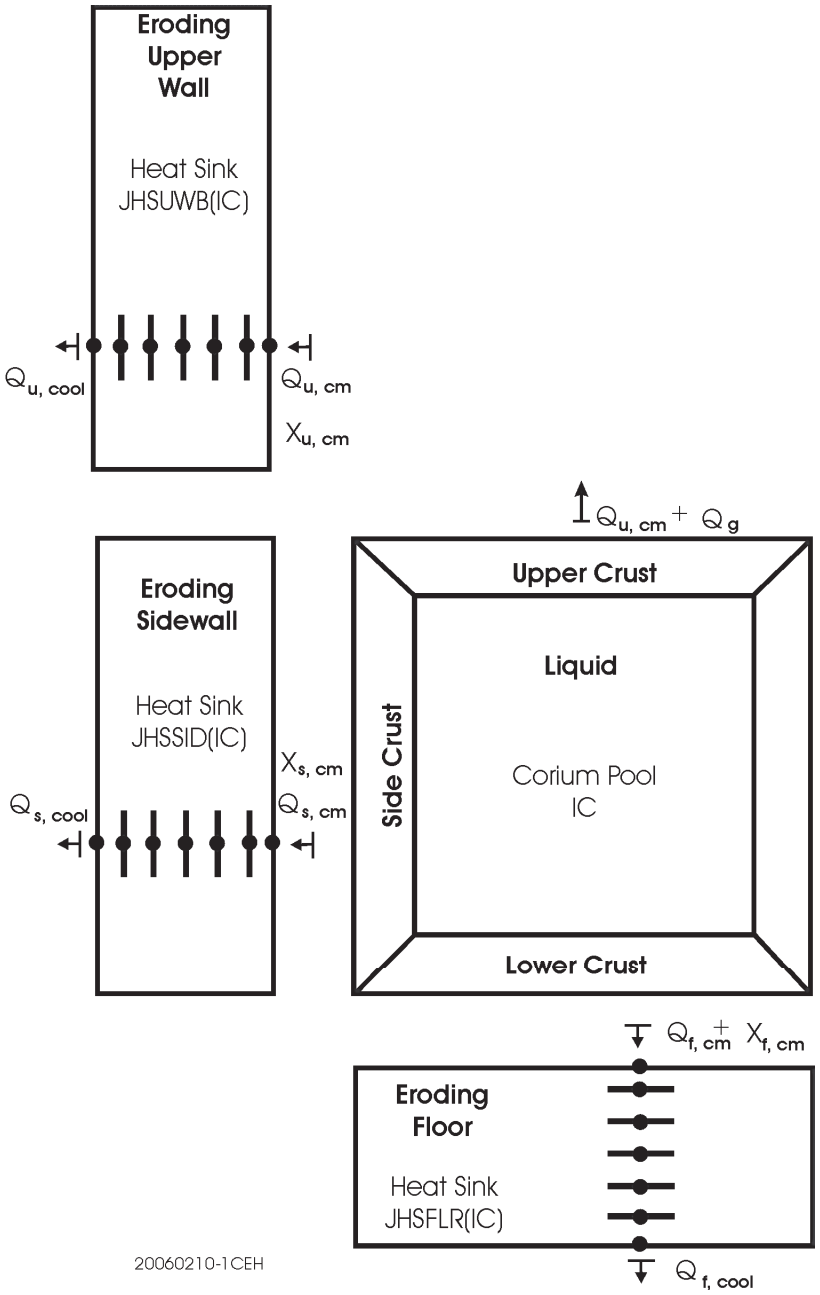


**Figure 2-1: MAAP 4.0.8 Model of Corium Pool, Crusts, and Concrete Slab**

**Q= Power and X= Eroded Distance**

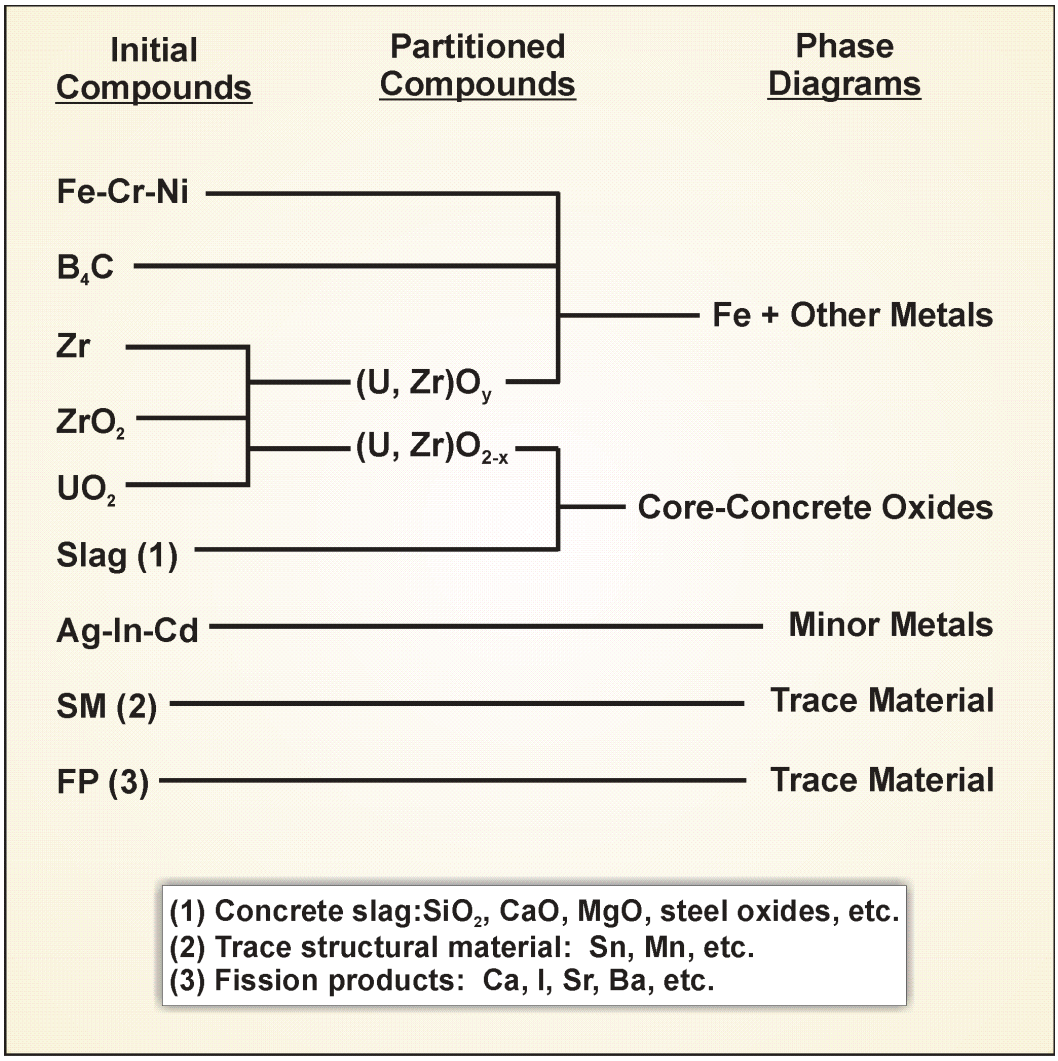


**Figure 2-2: Organization of Materials for Energy-Temperature Relations**

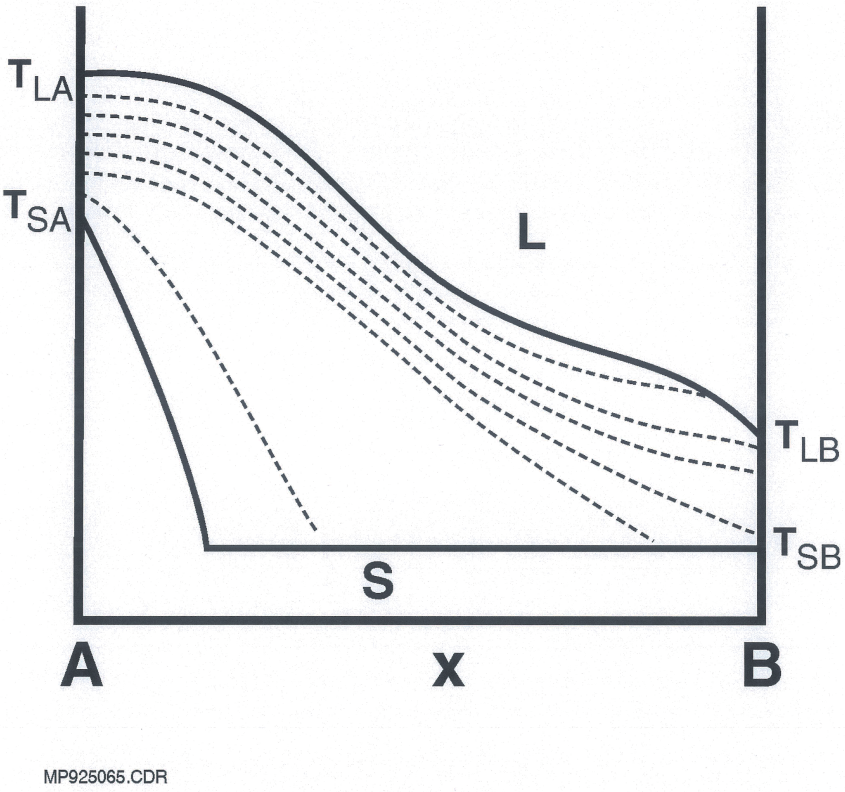


**Figure 2-3: Pseudo-Binary Phase Diagram with Dashed Lines Indicating Constant Liquid Fraction. Equilibrium composition pairs are not shown. For a selected bulk composition and temperature, the liquid fraction is found. This liquid fraction may be used together with an assumed solid (or liquid) composition to yield the liquid (or solid) composition.**

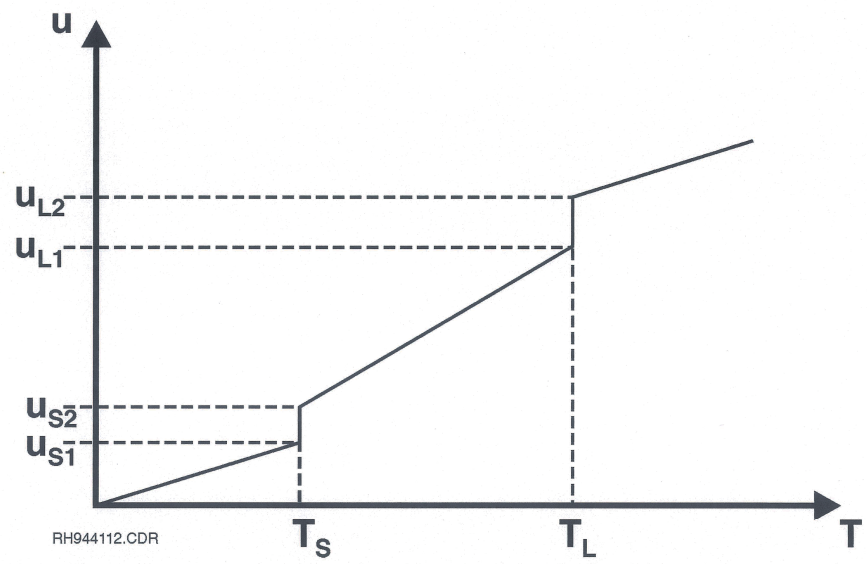


**Figure 2-4: Energy-Temperature Relationship for a Pseudo-Binary System**

**The slope in the two-phase range is, in general, not constant because the liquid fraction may vary non-linearly and because the latent heat depends upon the liquid composition. Note that partially congruent melting may occur at both the solidus and liquidus where the slope is vertical.**

**Table 2-3: MCCI Parameters Used in MAAP4.0.8 Analyses for APR1400**

TS

**Table 2-4: Additional Set of MCCI Parameters Used in Hydrogen Distribution and DDT Analyses for APR1400**

TS


**Figure 2-6: Ablation Depth in Cavity Floor for Different FCHF**


**Figure 2-7: Heat Flux from Corium to Water for Different FCHF**

TS

**Figure 2-8: Heat Transfer Rate from Corium to Water for Different FCHF**

TS

**Figure 2-9: Containment Pressure for Different FCHF**


**Figure 2-10: Comparison of Pressure in the Containment for the Cases with ENT0C=$10^{-5}$, and ENT0C=0.045**